

Quantitative microspectroscopic imaging reveals viral and cellular RNA helicase interactions in live cells

Received for publication, January 31, 2017, and in revised form, April 29, 2017 Published, Papers in Press, May 8, 2017, DOI 10.1074/jbc.M117.777045

M. J. Corby[†], Michael R. Stoneman[§], Gabriel Biener[§], Joel D. Paprocki[§], Rajesh Kolli[‡], Valerica Raicu^{§¶1}, and David N. Frick^{‡2}

From the Departments of [†]Chemistry and Biochemistry, [§]Physics, and [¶]Biological Sciences, University of Wisconsin-Milwaukee, Milwaukee, Wisconsin 53201

Edited by Norma Allewell

Human cells detect RNA viruses through a set of helicases called RIG-I-like receptors (RLRs) that initiate the interferon response via a mitochondrial signaling complex. Many RNA viruses also encode helicases, which are sometimes covalently linked to proteases that cleave signaling proteins. One unresolved question is how RLRs interact with each other and with viral proteins in cells. This study examined the interactions among the hepatitis C virus (HCV) helicase and RLR helicases in live cells with quantitative microspectroscopic imaging (Q-MSI), a technique that determines FRET efficiency and subcellular donor and acceptor concentrations. HEK293T cells were transfected with various vector combinations to express cyan fluorescent protein (CFP) or YFP fused to either biologically active HCV helicase or one RLR (*i.e.* RIG-I, MDA5, or LGP2), expressed in the presence or absence of polyinosinic-polycytidylic acid (poly(I:C)), which elicits RLR accumulation at mitochondria. Q-MSI confirmed previously reported RLR interactions and revealed an interaction between HCV helicase and LGP2. Mitochondria in CFP-RIG-I:YFP-RIG-I cells, CFP-MDA5:YFP-MDA5 cells, and CFP-MDA5:YFP-LGP2 cells had higher FRET efficiencies in the presence of poly(I:C), indicating that RNA causes these proteins to accumulate at mitochondria in higher-order complexes than those formed in the absence of poly(I:C). However, mitochondria in CFP-LGP2:YFP-LGP2 cells had lower FRET signal in the presence of poly(I:C), suggesting that LGP2 oligomers disperse so that LGP2 can bind MDA5. Data support a new model where an LGP2-MDA5 oligomer shuttles NS3 to the mitochondria to block antiviral signaling.

The term “helicase” was first used to describe enzymes that unwind DNA by separating Watson-Crick base pairs and untwisting the double helix (1). Such helicases function at the replication fork, forming oligomeric rings that surround one DNA strand while separating its complement, but they com-

prise only a small subset of all motor proteins that manipulate cellular nucleic acid structures. Ring helicases typically function as hexamers, in which each subunit contains a motor domain (2). ATP binds between the motor domains of adjacent subunits to initiate conformational changes leading to the movement of the helicase relative to the nucleic acid (3). Ring helicases are grouped into superfamilies (*i.e.* SF3³ and SF4) based on sequence homology; some translocate on DNA (*e.g.* the DnaB protein (4)), whereas others translocate on RNA (*e.g.* the Rho protein (5)). In contrast, helicases in superfamily 1 (SF1) and superfamily 2 (SF2) do not need to form rings because they possess two motor domains fused in tandem on the same polypeptide (6). Such non-ring helicases aid cellular DNA replication, DNA recombination, DNA repair, RNA processing, translation, viral RNA replication, and viral RNA detection. Although some SF1 and SF2 helicases function as monomers (7), biochemical evidence suggests that dimers or higher-order oligomers are also needed for optimal activity (8).

This study uses recombinant fluorescent fusion proteins, two-photon excitation quantitative microspectroscopic imaging (Q-MSI) (9, 10), which employs quantitative FRET (9–11) with dual excitation (*i.e.* two excitation wavelengths), and fully quantitative analysis (12, 13). Q-MSI demonstrated that viral and human RNA helicases form ordered complexes in cells. Four different RNA helicases, all members of the SF2, were used in this study (14). One of the helicases is the nonstructural protein 3 (NS3), which is encoded by the hepatitis C virus (15), whereas the other three are human cellular helicases that detect viral RNA and initiate the interferon response through the mitochondrial antiviral signaling protein (MAVS) (16). Collectively known as RIG-I-like receptors (RLRs), these proteins are RIG-I (retinoic acid-inducible gene 1), MDA5 (melanoma differentiation-associated protein 5), and LGP2 (Laboratory of Genetics and Physiology 2) (17–19). RLRs are a subset of innate immune system proteins called pattern recognition receptors that sense cellular invaders by recognizing nucleic acid, protein,

This work was supported by National Institutes of Health Grant RO1AI088001 (to D. N. F.), University of Wisconsin-Milwaukee Research Growth Initiative Grant 101X333 (to D. N. F. and V. R.), and National Science Foundation Major Research Instrumentation Program Grant PHY-1126386 (to V. R.). Dr. Raicu is a co-founder of Aurora Spectral Technologies LLC (AST), which commercializes OptiMiS technology used in this work. Dr. Stoneman was employed by AST in the past and occasionally consults for them. The content is solely the responsibility of the authors and does not necessarily represent the official views of the National Institutes of Health.

¹ To whom correspondence may be addressed. E-mail: vraicu@uwm.edu.

² To whom correspondence may be addressed. E-mail: frickd@uwm.edu.

³ The abbreviations used are: SF, superfamily; CARD, caspase recruitment domain; HCV, hepatitis C virus; ISRE, interferon-stimulated response element; MAVS, mitochondrial antiviral signaling protein; poly(I:C), polyinosinic-polycytidylic acid; ROI, region of interest; NLS, nuclear localization signal; Q-MSI, quantitative microspectroscopic imaging; EMCCD, electron-multiplying charge-coupled device; RIG-I, retinoic acid-inducible gene 1; RLR, RIG-I-like receptor; PAMP, pathogen-associated molecular pattern; CFP, cyan fluorescent protein; ER, endoplasmic reticulum; ANOVA, analysis of variance.

Viral and cellular helicase interactions

or carbohydrate epitopes, called pathogen-associated molecular patterns (PAMPs), not typically present in healthy cells. After pattern recognition receptors bind ligands, they initiate a signaling cascade resulting in the production of interferons, which alert neighboring cells and recruit other cells to the area of infection. RLRs bind RNA ligands present in viruses like duplex tracts or 5' termini lacking typical eukaryotic caps (20).

All four proteins used here share homologous helicase motor domains, including a DECH sequence in their ATP binding site (21, 22). Prior studies using cell extracts, X-ray crystallography, and other techniques have shown that NS3 (8, 23), RIG-I (24), MDA5 (22), and LGP2 (25) all form oligomers. Other studies have uncovered a key interaction between LGP2 and MDA5 (26, 27), and there is an interesting relationship between the RLRs and NS3. The NS3 helicase is part of a multifunctional protein that has an N-terminal protease domain that cleaves MAVS to block the interferon response (28, 29). RIG-I and MDA5 also interact with MAVS via their N-terminal caspase recruitment domains (CARDs). However, a direct interaction between NS3 and an RLR has not yet been demonstrated; nor has there been convincing evidence that RLR oligomerization occurs in living cells (30).

This project was initially designed to test the notion that homologous protein/protein interaction motifs shared between NS3 and RLRs enable the NS3 helicase domain to position the NS3 protease where it can cleave key cellular targets needed for the interferon response. For example, NS3 might locate MAVS by forming hetero-oligomers with RIG-I, MDA5, and/or LGP2. To test this hypothesis, we designed pairs of fluorescent fusion proteins (31, 32) to be used in cell-based FRET assays. Cyan fluorescent protein (CFP) (33) was used as the donor, and YFP (34) was used as the acceptor in FRET. Each protein was designed to best retain its biological activity and subcellular localization. Data revealed a new and possibly biologically relevant interaction between HCV NS3 helicase domain and LGP2. In addition, FRET data confirmed that *in vivo* RLR interactions occur at the mitochondria and that these interactions change in the presence of a PAMP.

Results

Biologically active fluorescent RNA helicases

Seven plasmids were constructed to encode CFP-NS3, CFP-RIG-I, CFP-MDA5, CFP-LGP2, YFP-RIG-I, YFP-MDA5, and YFP-LGP2. Each fusion protein was designed to be expressed under the control of a CMV promoter upon transfection of 293T cells. All proteins were tagged at the N terminus. Both NS3 and each of the RLRs are multifunctional proteins with complex domain structures. NS3 harbors a protease domain at its N terminus linked to its C-terminal helicase domain. The NS3 protease also requires cofactor NS4A for activity and proper cellular localization. The same HCV open reading frame encodes both NS3 and NS4A, with NS4A immediately downstream of NS3. Upon translation, NS4A binds NS3 to activate the protease, which cleaves the NS3/NS4A junction. NS4A then tethers NS3 to endoplasmic reticulum (ER) membranes as part of the viral replicase. The CFP-NS3 plasmid was therefore

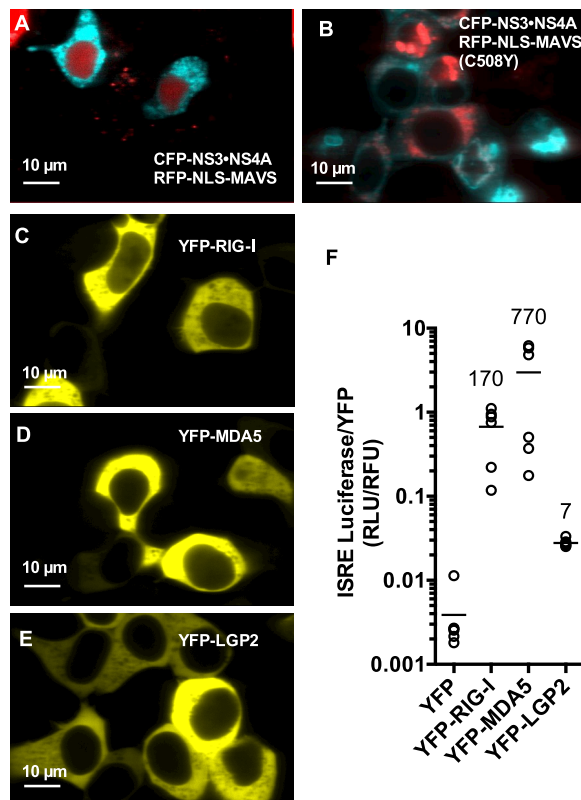


Figure 1. Ectopically expressed fluorescent helicase fusion proteins retain biological activity. A and B, ability of CFP-tagged NS3 to cleave a substrate. 293T cells were co-transfected with a plasmid expressing CFP-NS3-NS4A and either a plasmid expressing RFP-NLS-MAVs (A) or a plasmid expressing RFP-NLS-MAVs with the cleavage site mutation (C508Y) in the NS3 cleavage site (B). After 24 h, cells were imaged using a two-photon microscope. The cells were excited at 840 and 1,020 nm to target CFP and RFP, respectively. C–E, 293T cells were transfected with plasmids encoding either YFP-RIG-I (C), YFP-MDA5 (D), or YFP-LGP2 (E). After 24 h, the cells were excited at 960 nm to image YFP fluorescence. F, ability of YFP-RIG-I, YFP-MDA5, and YFP-LGP2 to signal an interferon response. 293T cells were co-transfected with plasmids encoding either YFP, YFP-RIG-I, YFP-MDA5, or YFP-LGP2 and a plasmid encoding firefly luciferase under the control of an ISRE promoter. Luciferase activity (relative luciferase units (RLU)) was normalized to YFP fluorescence (relative fluorescence units (RFU)) and is reported (bars represent means). Values above the bars report -fold stimulation relative to cells expressing YFP.

designed to encode full-length NS3 and NS4A proteins, with CFP fused to the NS3 N terminus. In transfected cells, such a protein formed clear foci in the cellular cytoplasm (Fig. 1A), suggesting that NS3 bound NS4A and that the membrane tether of NS4A was intact.

To probe CFP-NS3 activity, the cells were co-transfected with a second plasmid that encodes the MAVS NS3 cleavage site linked to an RFP with a nuclear localization signal (NLS). In the absence of NS3, this RFP-NLS-MAVS is expressed in the cytoplasm. However, upon cleavage by NS3, MAVS migrates to the cell's nucleus (35). In this assay, the CFP-NS3-NS4A complex retained the ability to cleave MAVS in cells (Fig. 1A). In a control assay, RFP-NLS-MAVS harboring a mutation (C508Y) in the NS3 cleavage site was expressed, and the CFP-NS3 complex did not cause the RFP to accumulate in the nucleus (Fig. 1B).

RIG-I and MDA5 each contain two CARD domains at their N terminus, followed by the helicase domain and a Zn²⁺-con-

taining regulatory C-terminal domain. LGP2 is similar, but it lacks the CARD domains. We therefore tagged each RLR protein at their N termini. Others have shown that similar N-terminal tags on RLRs do not affect functional interactions with their RNA ligands or downstream signaling ability (36–41). Each fluorescent RLR fusion protein used here expressed a cytoplasmic protein (Fig. 1, C–E).

When each RLR-expressing cell line was co-transfected with a second plasmid encoding firefly luciferase under the control of a promoter regulated by an interferon-stimulated response element (ISRE), the RLRs stimulated the promoter's activity (Fig. 1F), suggesting that each fluorescent fusion protein retained its signaling activity. As seen in Fig. 1F, LGP2 shows less ISRE signaling activity, which is expected due to its lack of CARDS, the presence of any ISRE stimulation in the presence of overexpressed LGP2 is attributable to an interaction between LGP2 and endogenous RLRs that contain CARDS.

FRET analysis reveals interactions between HCV NS3 and RLRs

The dual-excitation microspectral imaging technique (Q-MSI) (13), a fully quantitative FRET method recently developed to analyze interactions within ensembles of proteins in living cells (12, 13), was used here to determine the relative FRET efficiency (E_{app}) as well as the donor- and acceptor-labeled protein concentrations in selected regions of interest (ROIs). Q-MSI analyzes cells co-transfected with plasmids expressing both the donor (CFP) and acceptor (YFP) proteins excited at two wavelengths where pixel-level emission spectra are acquired for each of the two excitations (Fig. 2, C and D). The resulting “mixed” spectra are deconvoluted (*i.e.* unmixed) (42) using information obtained from similar scans of cells expressing either donor alone (Fig. 2A) or acceptor alone (Fig. 2B). Here, two-photon excitation was used to perform the “FRET scan,” with an excitation wavelength of $\lambda_{ex,1} = 840$ nm (Fig. 2C) and the “acceptor scan” with an excitation wavelength of $\lambda_{ex,2} = 960$ nm (Fig. 2D). Two excitation scans are needed to (i) account for direct excitation of YFP at $\lambda_{ex,1}$ and (ii) calculate the concentration of the donor and acceptor.

For each excitation scan, 200 2D fluorescence intensity images were collected, each representing the pixel-level intensities seen at wavelengths between ~ 400 and ~ 600 nm, with ~ 1 nm resolution. For a given field of view, the acquisition of the two excitation scans is completed in ~ 60 s: 10 s to acquire each set of spectral images and 40 s between the two scans to change the excitation wavelength of the laser. As discussed below, this method provides the apparent FRET efficiency, E_{app} , as well as CFP and YFP concentration. However, the elapsed time between the two excitations (40 s) allows for molecular diffusion and is therefore too long to generate pixel-level information. Therefore, E_{app} and concentrations were only computed as an average over an ROI (whole cell or subcellular ROI). This trade-off is necessary when the acceptor concentration also needs to be determined in FRET imaging.

The first step in Q-MSI involves calculating the individual contributions of donor and acceptor signals to an experimentally obtained composite spectrum. Assuming that the composite (mixed) spectrum is a linear combination of the contribu-

tions of the donor and acceptor spectra, factors are determined that scale the fluorescence of the acceptor in the presence of the donor (k^{AD}) and the fluorescence of the donor in the presence of the acceptor (k^{DA}) (see Equation 1) to fit the measured composite spectra (42). These factors were determined at two excitation wavelengths for each field of view. The first wavelength ($\lambda_{ex,1} = 840$ nm) excites CFP, and the second ($\lambda_{ex,2} = 960$ nm) excites YFP, in both cases through a nonlinear process known as two-photon excitation (43). These two factors, derived from spectral unmixing, were then used, along with the spectral integrals and standard curves generated from images of purified CFP and YFP (13, 44), to calculate E_{app} from Equation 4, donor concentration from Equation 2, and acceptor concentration from Equation 3 (see Fig. 2 and “Experimental procedures”).

Q-MSI analysis was first performed using CFP-NS3 as the donor and either YFP-RIG-I, YFP-MDA5, or YFP-LGP2 as the acceptor. Pairs were co-expressed in 293T cells via transient transfection. Most cells analyzed had E_{app} values near zero when either YFP-RIG-I or YFP-MDA5 was used as the acceptor. However, with YFP-LGP2 as the acceptor, about half of the cells analyzed showed some FRET, although E_{app} values were typically $< 20\%$ (Fig. 2, H and I).

When a similar set of transfections was performed using CFP-LGP2 as the donor, most cells expressing either YFP-RIG-I or YFP-MDA5 as the acceptor again showed no apparent FRET. However, when YFP-LGP2 was used as the acceptor, most cells showed some FRET. The average E_{app} seen in cells expressing LGP2 oligomers was 12%, and some cells had E_{app} values as high as 30% (Fig. 2, J and K).

To explore the NS3/LGP2 interaction in more detail, three different mutant constructs expressing various deletions in the CFP-NS3-NS4A sequence were generated and used to co-transfect 293T cells with the YFP-LGP2 plasmid. In the first mutant (scNS3-4A), the membrane localization regions of NS4A were removed, and the region of NS4A that activates NS3 was covalently attached between the NS3 N terminus and CFP. Such a protein retains cellular protease activity but fails to form foci like the full-length NS3-NS4A complex (Fig. 3, A and B). The second mutant (NS3), which did not contain NS4A, lacked the ability to cleave MAVS in cells and was distributed throughout the cytoplasm (Fig. 3C). The third mutant (NS3h) lacked the entire protease domain and was also broadly distributed throughout the cells (Fig. 3D). Despite these different properties, each protein retained an ability to interact with LGP2, suggesting that the interaction occurs via the NS3 helicase domain. Most cells displayed E_{app} values around 5%, but some had E_{app} values as high as 30%; the single-chain NS3-NS4A protein had the highest average E_{app} (Fig. 3, E and F).

When whole cells were selected as ROIs in the above experiments, it is possible that E_{app} values were biased toward lower values because ROIs contained many regions lacking fluorescent helicases (*e.g.* the nucleus). To examine this possibility, subcellular ROIs expressing CFP-NS3-4A were selected in cells that had been co-transfected with a CFP-NS3-NS4A plasmid and plasmids expressing YFP-tagged version of each of the RLRs (Fig. 3A). These subcellular ROIs were defined as the foci seen in 2D spatial distribution maps of k^{DA} (Fig. 4A). These foci should represent regions where NS3 is tethered to the ER mem-

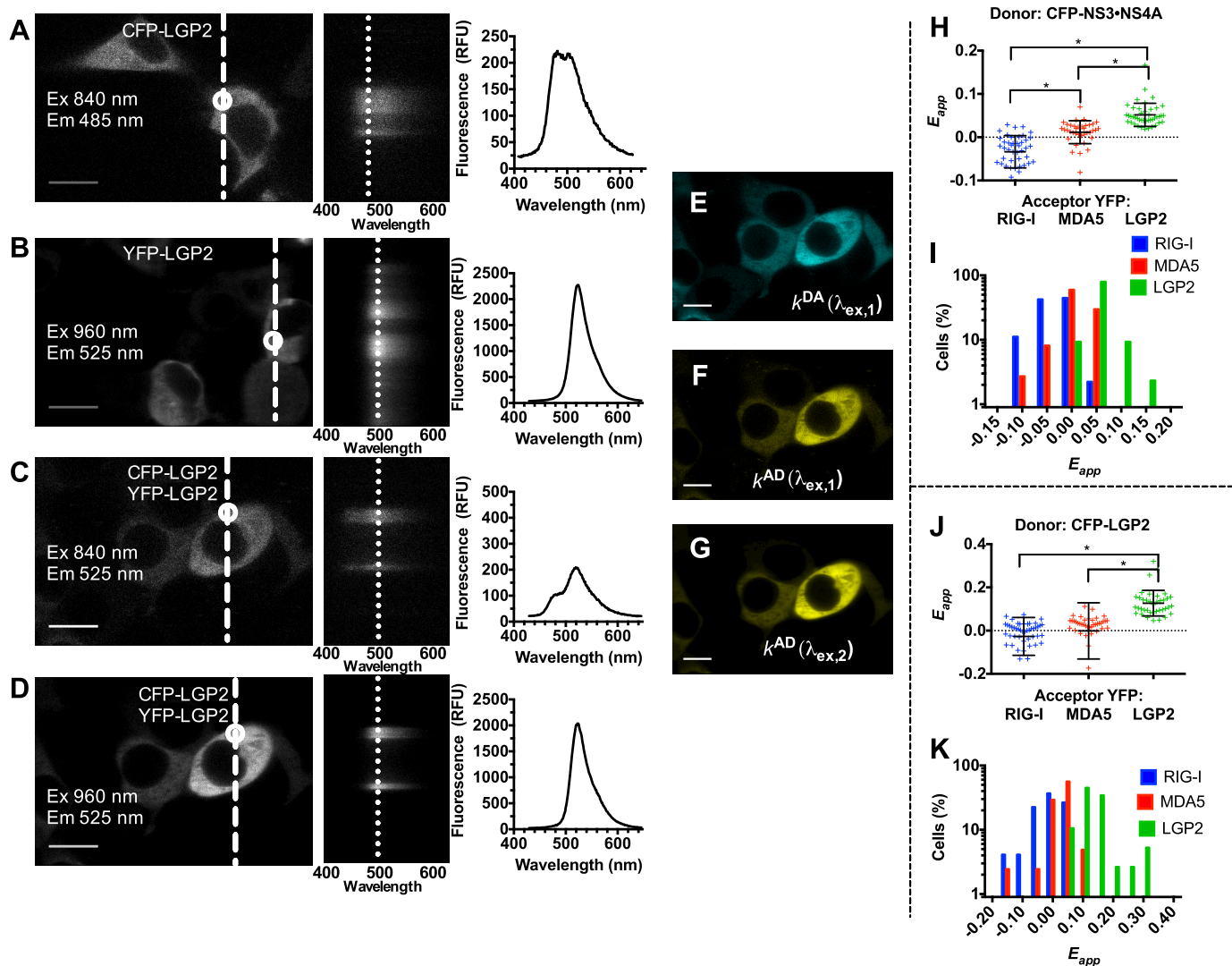
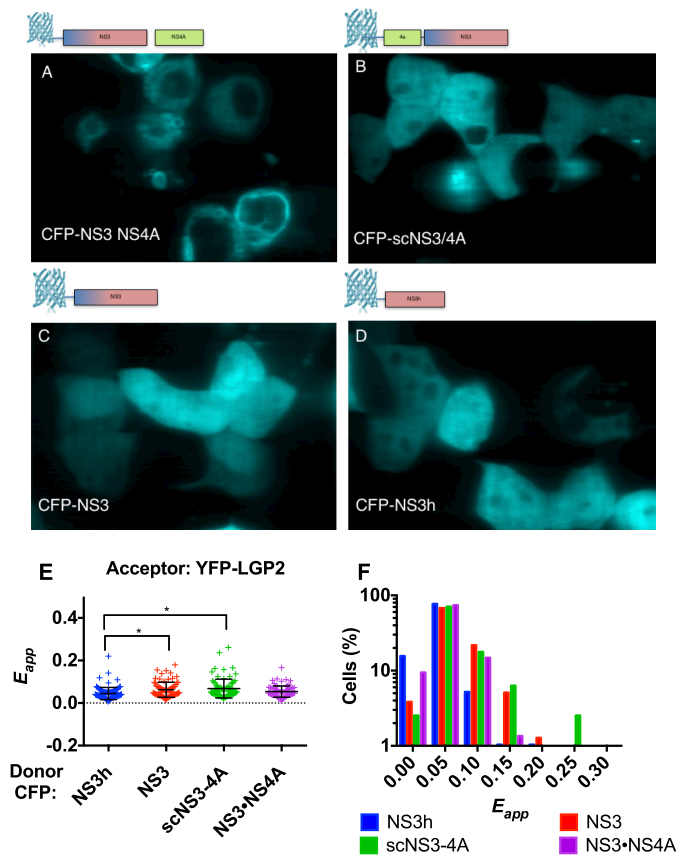


Figure 2. Whole-cell dual-excitation fluorescence microspectroscopy analysis of helicase interaction. 293T cells were transfected with a plasmid expressing either CFP-LGP2 (A) or YFP-LGP2 (B), or co-transfected with plasmids expressing both CFP-LGP2 and YFP-LGP2 (C and D). The cells were exposed to 840 nm ($\lambda_{ex,1}$) and 960 nm ($\lambda_{ex,2}$) ultrashort-pulse laser light and imaged using a two-photon microspectroscope (see “Experimental procedures”). 3D fluorescence images consisting of 2D fluorescence intensity maps (left panels) for 200 emission wavelengths (defining the third dimension; see “Experimental procedures”) were collected for each excitation wavelength. Images shown in each left-hand panel correspond to the wavelength where the maximum fluorescence emission was detected, the center panels show projections of the fluorescence emission in the spectral dimension (i.e. emission wavelength) corresponding to the dashed line in each left-hand panel, and the right-hand panels show the intensity scales of fluorescence as well as the average spectra for the circled ROIs shown in the left panels. Using the elementary spectra obtained from the CFP-LGP2 alone (A) and YFP-LGP2 (B), the stacks of 200 emission wavelengths (corresponding to the cells displayed in C and D) were unmixed (i.e. deconvoluted) at each pixel via a general least-squares minimization method described previously (see “Experimental procedures”) to yield a 2D spatial distribution map of donor fluorescence in the presence of acceptors (i.e. $k^{DA}(\lambda_{ex,1})$) (E) and a 2D spatial distribution map of acceptor in the presence of donor, $k^{AD}(\lambda_{ex,1})$ (F). To both correct for inadvertent excitation of the acceptor (YFP) by the donor excitation wavelength ($\lambda_{ex,1}$) and determine the concentration of acceptor over entire regions of interest, a second, “acceptor” scan was taken at the acceptor excitation wavelength ($\lambda_{ex,2}$). When the acceptor scan is spectrally unmixed (D), it yields the spatial distribution of acceptor molecules in the co-expressing sample (G). Regions of interest in the co-expressing sample were selected, which included both CFP and YFP signal. These selections were then used as a mask and applied to the $k^{AD}(\lambda_{ex,1})$, $k^{DA}(\lambda_{ex,1})$, and $k^{AD}(\lambda_{ex,2})$ images to calculate average E_{app} over the selected regions (assays with LGP2 are shown in A–G). H and I, FRET analysis of cells co-expressing CFP-NS3-4A and either YFP-RIG-I, YFP-MDA5, or YFP-LGP2. The scatter plot (H) shows the mean \pm S.D. (error bars). E_{app} values calculated for each cell, which were, in order, -0.034 ± 0.04 , 0.012 ± 0.027 , and 0.052 ± 0.027 . A one-way ANOVA revealed a significant main effect of group ($F(2,122) = 84.07$, $p < 0.0001$), and Tukey post-hoc tests showed that each group differed significantly from the others (* , $p < 0.0001$). The histogram (I) shows the spread of the E_{app} values for each combination in steps of 0.05. J and K, FRET analysis of cells co-expressing CFP-LGP2 and either YFP-RIG-I, YFP-MDA5, or YFP-LGP2, shown as in H and I. The E_{app} means and S.D. values were, in order, -0.027 ± 0.084 , -0.001 ± 0.130 , and 0.127 ± 0.059 . The significant one-way ANOVA ($F(2,125) = 29.40$, $p < 0.0001$) was driven by the fact that the LGP2 group differed significantly from the RIG-I and MDA5 groups (* , $p < 0.0001$). The RIG-I and MDA5 groups did not differ from each other.

brane by NS4A. Such a detailed analysis revealed average E_{app} values similar to those seen in the whole-cell analyses (Fig. 2, H, I). Most ROIs with RIG-I and MDA5 had no FRET, and the average FRET seen with LGP2 was about 5%. However, this subcellular analysis revealed a subset of regions with notably higher FRET. For example, seven ROIs were found where FRET

was seen between NS3 and RIG-I (between 10 and 40% E_{app}). Although some FRET was seen between RIG-I and NS3, FRET efficiency was still clearly higher between NS3 and LGP2. To better understand how reproducible this effect was, the measurement and analysis of cells co-transfected with CFP-NS3-4A and LGP2 was repeated, and an additional set of 222 ROIs were



analyzed. Indistinguishable results were obtained in the repeat experiments (Fig. 4, C and D).

Subcellular Q-MSI analysis reveals RLR responses to poly(I:C)

Q-MSI was next used to examine the current models, which suggest that RLRs respond to viral PAMPs by forming signaling complexes at the mitochondrial membranes with MAVS (45). If such models are correct, one would expect to see the fluorescent RLRs accumulate at the mitochondria. To test this hypothesis, the mitochondria of cells co-transfected with RLR combinations were stained with MitoTracker Red, a dye that fluoresces in a spectral region distinct from CFP and YFP. The

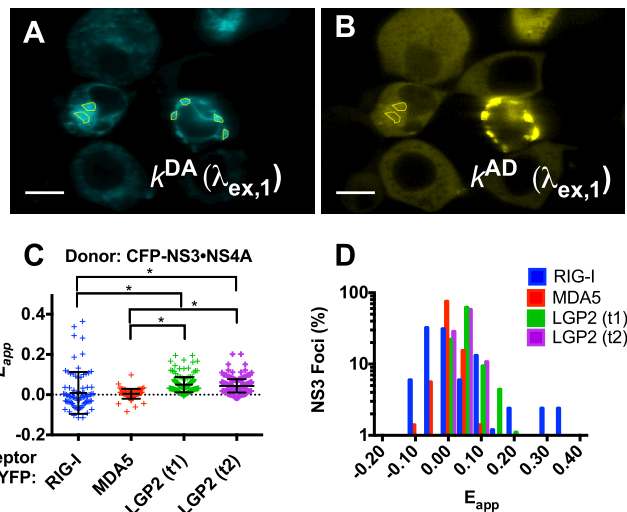


Figure 4. Subcellular fluorescence microspectroscopy analysis of NS3 helicase interaction. 293T cells co-transfected with plasmids encoding CFP-NS3-NS4A complex and one of the following: YFP-RIG-I, YFP-MDA5, or YFP-LGP2. After 24 h, cells were analyzed as in Fig. 2 except that subcellular regions (highlighted) were selected rather than whole cells. A, 2D spatial distribution map of CFP-NS3-NS4A fluorescence in the presence of acceptors, $k^{DA}(\lambda_{ex,1})$. B, 2D spatial distribution map of YFP-LGP2 in the presence of donor, $k^{AD}(\lambda_{ex,1})$. C, scatter plot (plus symbols) shows the E_{app} value calculated for each ROI. The average $E_{app} \pm$ S.D. (error bars) and number of ROIs analyzed (n) (in order) were as follows: 0.009 \pm 0.10 ($n = 83$), 0.004 \pm 0.024 ($n = 71$), 0.050 \pm 0.038 ($n = 180$), and 0.044 \pm 0.033 ($n = 222$). One-way ANOVA revealed a significant main effect of group ($F(3,552) = 23.19, p < 0.0001$). Tukey post-hoc tests showed that both RIG-I and MDA5 were significantly different from LGP2(t1) and LGP2(t2) (*, $p < 0.0001$). D, histogram showing the number of ROIs expressing each E_{app} value (bin width = 0.1).

dye was used to find mitochondrial regions, which were selected for Q-MSI (Fig. 5). To identify mitochondria-localized YFP and CFP, the spectra obtained with cells expressing CFP (Fig. 5A) or YFP (Fig. 5B) or cells stained with MitoTracker (Fig. 5C) were used to unmix spectra obtained in MitoTracker-stained cells expressing both CFP and YFP (Fig. 5D). The ROIs were then identified on the resulting k^{DA} (Fig. 5E) and k^{AD} (Fig. 5F) maps by creating masks on the k^M 2D map (Fig. 5G).

In the first set of experiments, cells were co-transfected either with plasmids expressing CFP-RIG-I and YFP-RIG-I or with plasmids expressing CFP-MDA5 and YFP-MDA5. Some of these cells were then exposed to poly(I:C) RNA (0.36 μ g/ml in cell growth medium), and others were exposed to TurboFect only. RIG-I and MDA5 have both been shown to localize to MAVS at the mitochondrial membrane in response to poly(I:C) (46). Q-MSI imaging revealed clear differences upon the addition of the poly(I:C). Although the average E_{app} of mitochondria only changed from 3% to 4% for RIG-I upon the addition of poly(I:C) (Fig. 6B), a new, albeit very small, population of mitochondria was observed with E_{app} values ranging from 50 to 90%; these mitochondrial regions exhibiting high FRET values possibly indicate the location of RIG-I complexes not observed in the absence of poly(I:C).

Cells expressing CFP-MDA5 and YFP-MDA5 developed a larger population of mitochondria-localized MDA5 complexes in response to poly(I:C) stimulation (Fig. 6C). Note that the broad distributions of FRET efficiency values obtained are not necessarily caused by experimental errors; rather, they are indicative of the presence of relatively large oligomers compris-

Viral and cellular helicase interactions

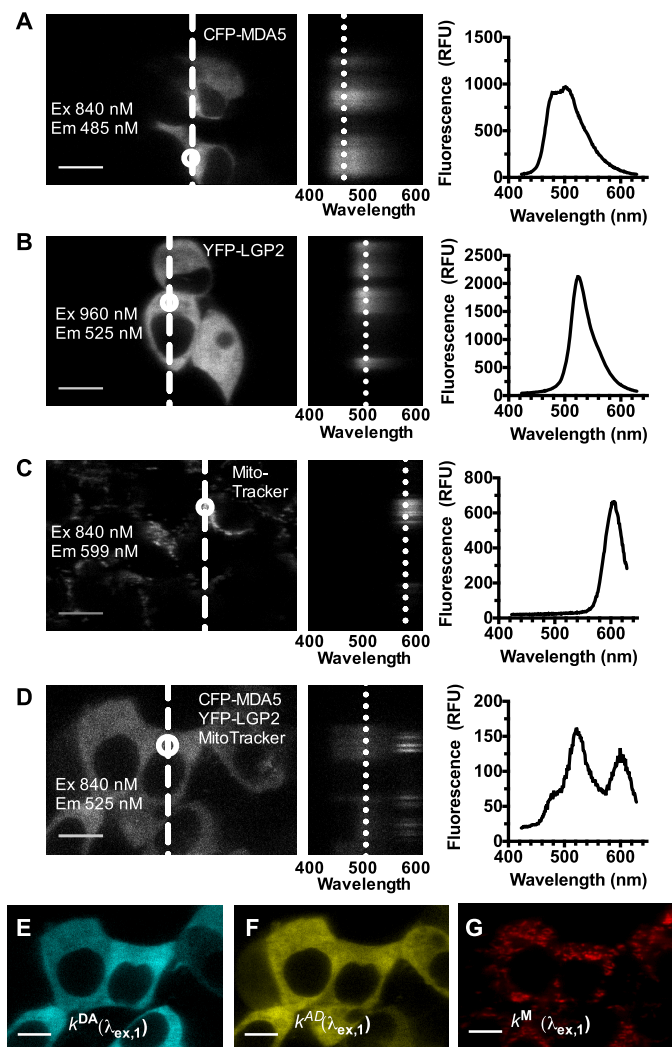


Figure 5. Subcellular dual-excitation fluorescence microspectroscopy analysis of cells expressing fluorescent donors, acceptors, and MitoTracker molecules. Before imaging, when necessary, the cells were stained with 25 ng/ml MitoTracker Red for 20 min. Cells expressing only CFP-MDA5 (A) or only YFP-LGP2 (B) and cells expressing no fluorescent protein but stained with MitoTracker (C) were imaged, and selected ROIs were used to generate elementary spectra of CFP, YFP, or MitoTracker Red. These spectra were used to unmix the composite fluorescent spectra in cells presenting all three types of fluorescence signals. D, the three-component unmixing has been introduced before (13) and summarized under “Experimental procedures.” The spectra on the right correspond (from top to bottom) to donor-only, acceptor-only, MitoTracker-only, and a typical composite spectrum including contributions from all three fluorophores (taken from the mitochondrial region). E, 2D spatial distribution map of donor fluorescence in the presence of acceptors $k^{DA}(\lambda_{ex,1})$. F, 2D map of acceptor fluorescence in the presence of donor $k^{AD}(\lambda_{ex,1})$. G, 2D map of MitoTracker $k^M(\lambda_{ex,1})$ intensity.

ing different combinations of donors and acceptors and hence a distribution of different FRET efficiencies (see Refs. 11 and 44 and “Discussion”).

As a control, we performed the same subcellular analysis using cells co-transfected with plasmids expressing CFP-LGP2 and YFP-LGP2. Because LGP2 lacks CARDs, one would not expect it to accumulate at the mitochondria to the same extent as RIG-I or MDA5. Not surprisingly then, unlike RIG-I and MDA5, an increase in FRET efficiency was not seen with LGP2 (Fig. 6D); nor was a new subpopulation of regions with high FRET noted (Fig. 6D). In fact, lower FRET efficiencies were

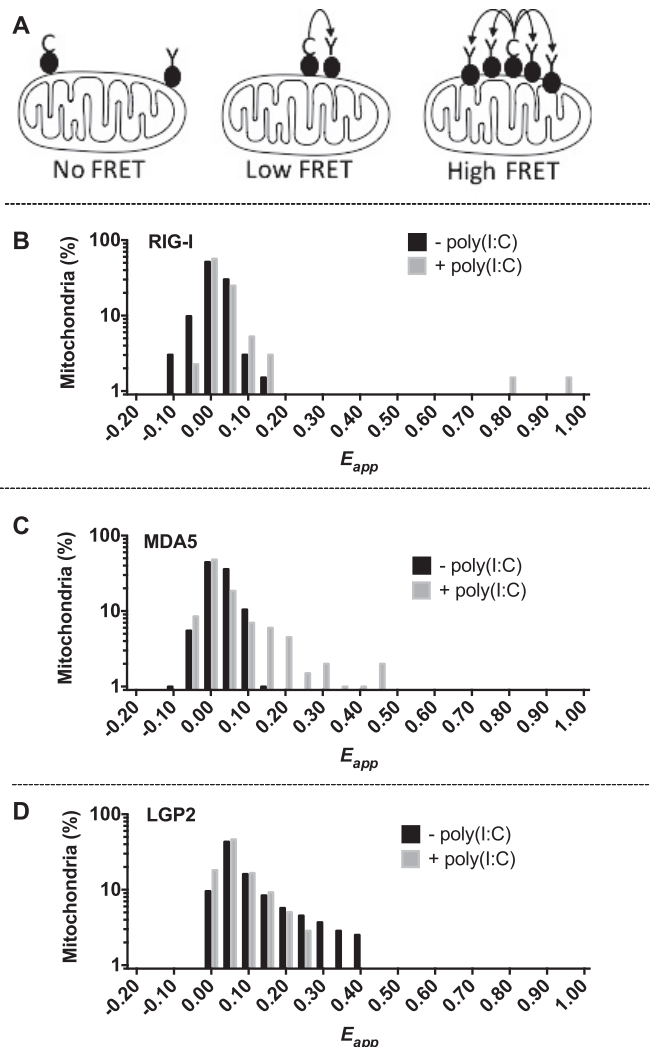


Figure 6. Response of mitochondrial RIG-I, MDA5, and LGP2 to poly(I:C) exposure. A, expected FRET from mitochondrial CFP and YFP-tagged RLRs if proteins interact as dimers or higher-order oligomers. In each experiment, cells were exposed to poly(I:C) (0.36 μ g/ml in media) 4 h before imaging. The cells stained with MitoTracker were then subjected to Q-MSI analysis, in which mitochondrial ROIs were selected using the MitoTracker signal as a mask, and the average E_{app} for each ROI was calculated. B, Q-MSI analysis of cells co-transfected with plasmids encoding YFP-RIG-I and CFP-RIG-I. The histogram shows the number of mitochondrial ROIs producing each E_{app} value, in steps of 0.05 (132 ROIs were randomly selected for each set). A Brown-Forsythe test was performed and yielded a p value < 0.01. C, Q-MSI analysis of cells co-transfected with plasmids expressing YFP-MDA5 and CFP-MDA5 and treated the same as cells in B (200 ROIs were randomly selected for each set). A Brown-Forsythe test was performed and yielded a p value < 0.001. D, Q-MSI analysis of cells co-transfected with plasmids expressing YFP-LGP2 and CFP-LGP2 and treated the same as cells in B (593 ROIs were randomly selected for each set). A Brown-Forsythe test was performed and yielded a p value < 0.001.

seen, suggesting that some of the LGP2 oligomers in these subcellular ROIs might have dissociated. One possibility is that LGP2 instead interacted with another protein like endogenous MDA5, as has been reported before (27). Then the addition of poly(I:C) may have stimulated the expression of more endogenous MDA5, which in turn caused formation of hetero-oligomers containing lower proportions of exogenous (*i.e.* fluorescently labeled) LGP2 to endogenous MDA5.

To examine the LGP2 interaction with overexpressed exogenous (*i.e.* fluorescently labeled) MDA5 (47), cells were co-transfected with plasmids expressing CFP-LGP2 and YFP-

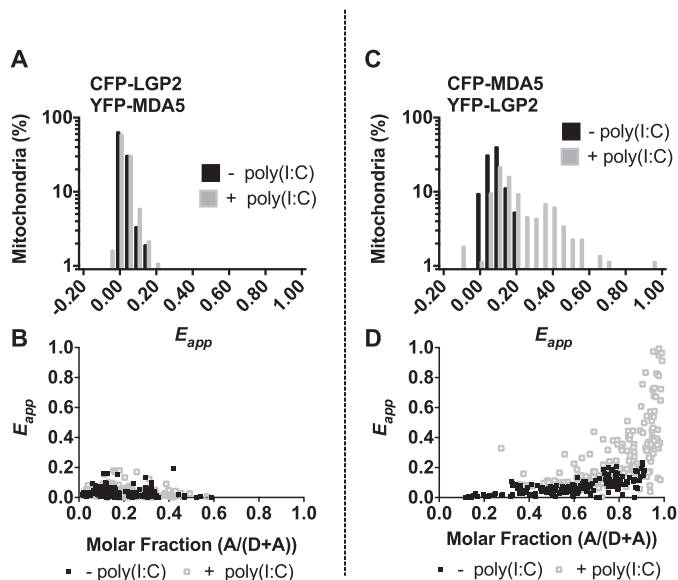


Figure 7. Analysis of MDA5/LGP2 interaction in the presence and absence of poly(I:C). A, FRET analysis of cells co-expressing CFP-LGP2 and YFP-MDA5 with and without poly(I:C) transfection. 293T cells were co-transfected with CFP-LGP2 and YFP-MDA5 plasmids. The cells were incubated for 20 h and then transfected with either 0.36 $\mu\text{g/ml}$ poly(I:C) or vehicle. At 24 h, the cells were stained with 25 $\text{ng}/\mu\text{l}$ of MitoTracker Red for 20 min, after which they were imaged at 100 \times using a two-photon microspectroscopy. The cells were successively excited at 840 and 960 nm, yielding two stacks of images. The composite spectra were unmixed, regions of interest were selected in each image, and the average E_{app} for the region was calculated. The histogram (A) shows the spread of the E_{app} values with and without poly(I:C) (210 ROIs were randomly selected for each set). The Brown-Forsythe test was performed and yielded a p value of 0.03. B, E_{app} values versus the molar fraction of acceptor molecules with and without poly(I:C). C and D, FRET analysis of cells co-expressing CFP-MDA5 and YFP-LGP2 (430 ROIs were randomly selected for each set). The experimental method and analysis used for C and D was identical to that corresponding to A and B. A Brown-Forsythe test was performed and yielded a p value < 0.001 .

MDA5. In the absence of poly(I:C), such cells displayed some interaction, with E_{app} ranging from zero to $\sim 20\%$, confirming that an MDA5-LGP2 complex forms in live cells on or near the mitochondria (Fig. 7, A and B). When poly(I:C) was added, a somewhat larger number of mitochondria exhibited relatively high FRET efficiencies (Fig. 7, A and B). This increase was probably caused by the fact that more exogenous, labeled MDA5 localized to the mitochondrial membrane, therefore allowing for more FRET-productive complexes to form. The more heterogeneous distribution of mitochondrial FRET values in the presence of poly(I:C) could be accounted for by the fact that poly(I:C) only reaches a subpopulation of cells, due to the limits of transfection and the confines imposed by cellular transport and cell heterogeneity.

In the majority of mitochondrial ROIs sampled, there was a higher concentration of LGP2 than MDA5, as evidenced by the large number of ROIs with molar fraction values < 0.5 (see Fig. 7B). To confirm this observation, the fluorescent tags on LGP2 and MDA5 were switched, and the FRET experiment was repeated. YFP-LGP2 and CFP-MDA5 were co-expressed and stimulated with poly(I:C). The mitochondria were again identified using MitoTracker, and an average E_{app} for each mitochondrial region was calculated. Most mitochondria expressing YFP-LGP2 and CFP-MDA5 exhibited molar fraction values > 0.5 , confirming that LGP2 was in higher abundance in the

mitochondrial ROIs than the MDA5 (Fig. 7, C and D). Once again, the addition of poly(I:C) resulted in the creation of a large subpopulation of mitochondria with higher E_{app} compared with the cells without poly(I:C). These findings indicated that poly(I:C) stimulated interaction between LGP2 and MDA5.

Q-MSI reveals response of NS3-NS4A co-expressed with LGP2 to poly(I:C)

To understand the functional significance behind the LGP2 and NS3 helicase interaction, the CFP-NS3-NS4A plasmid was co-transfected in 293T cells along with YFP-LGP2. After 24 h of expression, the cells were either treated with poly(I:C) (0.36 $\mu\text{g/ml}$ in media) or vehicle. The resulting cells were imaged using successive 840- and 960-nm excitations, and the results were analyzed via Q-MSI. Whole cells were circled, and the average E_{app} was calculated. The histogram (Fig. 8A) shows a shift in E_{app} values with the addition of poly(I:C). Specifically, the addition of poly(I:C) increased the interaction of NS3-4A and LGP2 from an average of 5% to 7%. The concentrations (micromolar) of the CFP and YFP in each ROI were also calculated and ranged from 0.1 to 25 μM for both donor and acceptor in each experiment. A subpopulation of cells with notably lower concentrations of exogenous CFP and YFP was observed, however, in the cells treated with poly(I:C). Low protein levels would be expected if poly(I:C) treatment initiates an interferon-induced repression of translation (Fig. 8, B and C).

Last, the mitochondria of cells co-expressing CFP-NS3-4A and YFP-LGP2 were stained with MitoTracker Red and then imaged. The MitoTracker Red stain was then used to create a mask of mitochondrial regions, and this mask was applied to the CFP-NS3-NS4A and YFP-LGP2 intensity maps. Q-MSI was used to calculate the E_{app} . The histogram of FRET values at the mitochondria (Fig. 8D) shows an increase in average FRET from 7.7% to 8.2%. Although the histogram shows a shift in values away from the original population without poly(I:C) treatment toward higher FRET values with poly(I:C) treatment, the difference is not statistically significant.

Discussion

RNA helicases have been suspected to form oligomers in cells based on a variety of biochemical evidence obtained mainly using purified proteins. For example, NS3 and each RLR can be seen to form long oligomers using native PAGE and electron microscopy (26, 48–50). To examine whether such complexes form in cells, this study used ectopically expressed fluorescent fusion proteins and fully quantitative FRET imaging, which was recently developed to probe protein/protein interactions in living cells (11, 12). Interestingly, little self-interaction was seen with RIG-I or MDA5, but clear interactions were visible with LGP2, suggesting that, in the absence of a PAMP, only LGP2 forms an oligomer in the cytoplasm (Figs. 2 and 6). In the presence of poly(I:C), clear oligomer formation was seen with both MDA5 and RIG-I. An interaction between MDA5 and LGP2 was also confirmed here, with data supporting the current models in which LGP2 primes MDA5 assembly on RNA PAMPs to stimulate signaling whereas, at the mitochondria, excess LGP2 binds additional MDA5 regions to repress signaling (22, 27). LGP2 was also the only RLR that appeared to inter-

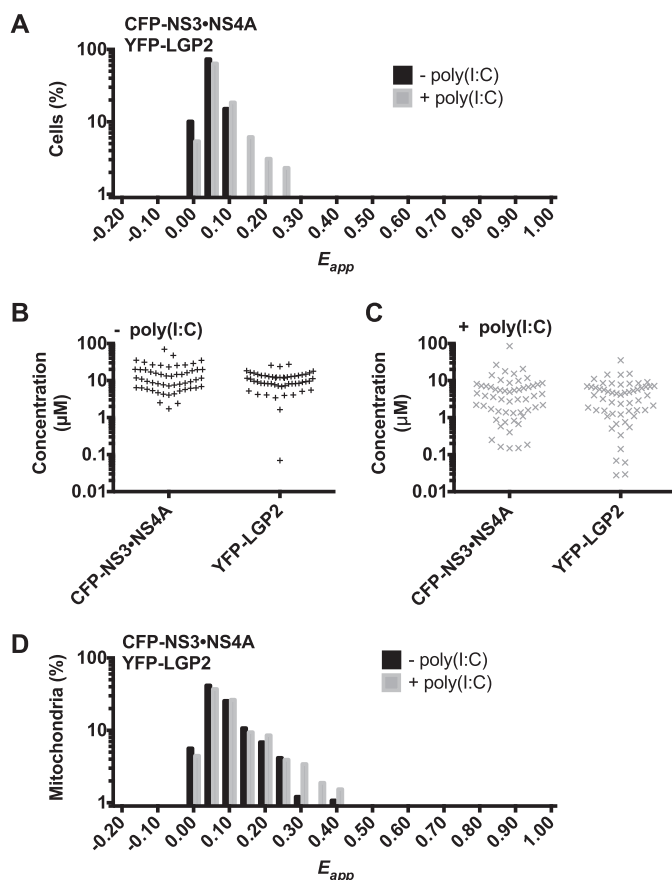


Figure 8. Analysis of NS3-4A and LGP2 interaction in the presence and absence of poly(I:C). A, FRET analysis of cells co-expressing CFP-LGP2 and YFP-MDA5 with and without poly(I:C) transfection. 293T cells were co-transfected with CFP-LGP2 and YFP-MDA5 plasmids. The cells were incubated for 20 h and then transfected with either 0.36 $\mu\text{g}/\text{ml}$ poly(I:C) or vehicle. The cells were successively excited at 840 and 960 nm, yielding two stacks of images. The composite spectra were unmixed, regions of interest were selected in each image, and the average E_{app} for the region was calculated. The histogram (A) shows the spread of the E_{app} values with and without poly(I:C). A Brown-Forsythe test was performed and yielded a p value < 0.01 . B, concentrations of CFP-NS-NS4A and YFP-LGP2 in cells not treated with poly(I:C). C, concentrations of CFP-NS-NS4A and YFP-LGP2 in cells treated with poly(I:C). D, to further understand the NS3-4A and LGP2 interaction, cells expressing YFP-LGP2 and CFP-NS34A were either mock-transfected or transfected with poly(I:C). The mitochondria were stained with MitoTracker Red and circled. The histogram shows the number of mitochondrial ROIs expressing each E_{app} value (bin width = 0.05). A Brown-Forsythe test was performed and yielded a p value of 0.344.

act with the HCV helicase, suggesting that LGP2 is a key multifaceted interaction partner in the innate immune system.

One advantage of Q-MSI over other techniques is its ability to calculate the precise fluorescent protein concentrations in cells and/or regions being analyzed. Because plasmids can express proteins at very high concentrations in some cells, low-affinity interactions might be observed that do not occur in nature. However, because Q-MSI allows for concentration calculation, it is possible to selectively analyze cells with high and low protein expression levels. In the experiments here, cellular concentrations of the fusion proteins ranged between 0.01 and 50 μM (Fig. 8, B and C). In all experiments, high E_{app} levels were observed even in cells with relatively low expression, and E_{app} did not correlate with an increase in total fusion protein concentration, suggesting that the interaction observed did not

simply result from overexpression. Instead, some correlation between the acceptor molar fraction and E_{app} was observed (Fig. 7, B and D), indicative of the interactions occurring in ensembles of oligomeric complexes.

Because recombinant purified NS3 (7, 23, 50), RIG-I (49), MDA5 (48), and LGP2 (26, 51) can all form filaments on RNA *in vitro*, the observation here that only a few of these proteins interact in cells to produce FRET was somewhat surprising. It is important to recognize, however, that such negative results do not rule out the possibility of interactions because, among other possibilities, the CFP and YFP might disguise necessary interacting motifs, or the fluorophores might be oriented such that they are too far for FRET to efficiently occur. The low FRET seen with RIG-I might be important (Fig. 6), however, given the recent observation that only monomeric forms of RIG-I were observed in cells, even in the presence of poly(I:C) and 5'ppp-dsRNA PAMPs (30). This absence of observed FRET does not disprove an interaction, and it is possible that interactions that were not observed occur in cells. Nevertheless, one way to test whether the fluorescent proteins mask interaction motifs would be to fuse them to other regions of the helicases. Another option would be to use small tags that bind small-molecule fluorophores (52). We are presently exploring both options but have yet to find additional fluorescent constructs that express active helicases in cells.

It is noteworthy that FRET was only observed between CFP-RIG-I and YFP-RIG-I when their interactions were analyzed at the mitochondria in the presence of poly(I:C) (Fig. 6). Remarkably, far more FRET was seen with CFP-MDA5 and YFP-MDA5 than CFP-RIG-I and YFP-RIG-I under the same conditions (Fig. 6). We had expected to see more FRET with RIG-I under these conditions because FRET has been previously observed between labeled RIG-I and MAVS when they are ectopically expressed in 293T cells (53) and because the CARDs of MAVS and RIG-I formed a helical tetrameric structure in a recent crystal structure of the complex (24). A close examination of the MAVS·RIG-I helical tetramer (Protein Data Bank file 4P4H) suggests that the N termini of RIG-I might actually be positioned separately in such a way that only low FRET is possible between the fusion partners. In the complex, the RIG-I CARDs appear to alternate with MAVS CARDs.

Because MDA5 and RIG-I have similar CARDs, one might expect that MDA5 would form a similar helical tetramer with MAVS as was seen with RIG-I (24). Our data suggest that is not the case. From our data, MDA5 oligomers at the mitochondria seem clearly different from RIG-I oligomers (Fig. 6). This might mean that MDA5·MAVS complexes place their N-terminal CARDs closer to one another than is seen with RIG-I or that MDA5 CARDs do not alternate systematically with MAVS CARDs. Alternatively, the RIG-I·MAVS complexes might not be as long-lasting as MDA5·MAVS complexes. Regardless, the MDA5 CARDs do not seem to form the same type of oligomers with MAVS as RIG-I CARDs.

The hetero-interaction observed here that has also been studied in most detail previously is the one between LGP2 and MDA5 (22, 25–27, 54, 55). The greatest FRET efficiencies seen in this Q-MSI study were observed between LGP2 and MDA5 (Fig. 7; see also Fig. 1F, where signaling is evident with LGP2

despite lacking CARDs). When YFP-LGP2 was co-expressed with CFP-MDA5 and stimulated with poly(I:C), the response was remarkable. Without poly(I:C), there was a small population of mitochondria with E_{app} values around 10%. With the addition of poly(I:C), this population shifted toward higher E_{app} values (around 20%). This finding is contrary to the current models, where LGP2 simply primes MDA5 filament formation (22). Rather, we might be observing complexes formed at LGP2 concentrations where LGP2 has been seen to inhibit MDA5 (27). Because we still do not know the stoichiometry of the LGP2-MDA5 complexes observed, it is not possible to design molecular models needed for further analysis of our FRET data. At this time, these data simply further reinforce the notion that LGP2 can attenuate MDA5 filament length (26).

When MDA5 was expressed alone, it showed essentially no FRET, which suggested that it undergoes no significant oligomerization. By contrast, when LGP2 was expressed alone, most of the cells exhibited significant FRET (e.g. $E_{app} = 0.12 \pm 0.06$ for the experiment reported in Fig. 2J), indicating the presence of oligomers. Strikingly, when poly(I:C) was added, the LGP2 FRET essentially disappeared (Fig. 6C), whereas that of MDA5 became higher (Fig. 6B). This suggested that poly(I:C) either decreases the binding strength between LGP2 protomers within an oligomer or increases the affinity of binding between individual LGP2 protomers and a different molecule, such as endogenous MDA5. It is also possible that a more prosaic effect is at play; poly(I:C) might somehow interfere with the position or orientation of the fluorescent tags, which are tethered rather flexibly to the helicases, in a manner that reduces the FRET efficiency for one pair and increases it for another. It is also possible that poly(I:C) is mediating the interaction, and it is not a direct protein/protein interaction. However, these effects should not affect only LGP2.

When combining the results from the FRET investigations of LGP2 and MDA5 expressed alone *versus* co-expressed, as outlined in the above paragraphs, a single coherent picture emerges: that poly(I:C) leads to association, at the mitochondria, of LGP2 with endogenous or exogenous MDA5. This conceptual model should be further tested, for instance, by using the FRET spectrometry approach developed previously to assess the stoichiometry of protein/protein interactions. FRET spectrometry has already been rigorously tested, using multiplexed model fluorescent proteins (56), and applied to investigations of the quaternary structure in living cells of an array of different membrane and cytoplasmic proteins, such as a bi-component bacterial ABC transporter (57), muscarinic M3 acetylcholine receptor (58), σ -1 receptor (44), and human opsin (59).

Of the two hetero-interactions that were observed here (LGP2/MDA5 and NS3/LGP2), the NS3/LGP2 interaction has not been reported before. This interaction could be biologically relevant if it somehow assists the NS3 protein in finding targets like MAVS. Foy *et al.* (60) initially probed the role of the NS3 helicase in MAVS cleavage by using a mutant NS3 protein lacking its helicase function (W501A). NS3 W501A retains the ability to block IRF-3 activation, meaning that the protein probably still cleaves MAVS. Later, Horner *et al.* (61) showed that the first α helix at the NS3 N terminus is critical for MAVS cleavage. The helix works with NS4A to help tether the NS3 to the

ER. The same study also showed that NS3 lacking a helicase domain is sufficient for MAVS cleavage when ectopically expressed in cells. We had nevertheless expected that an interaction might occur between RIG-I and NS3 because of the key role that RIG-I plays in detecting HCV and because other viral proteins have been seen to interact with RIG-I. Cells without wild-type RIG-I (called Huh 7.5) allow better HCV replication (62), and RIG-I interacts with nonstructural protein 1 (NS1) encoded by influenza A virus, as was shown using similar techniques, cells, and protein constructs as used here (37, 38). It is possible that LGP2 might instead help shuttle NS3 to cellular regions containing MAVS because LGP2 also interacts with MDA5, which binds MAVS upon activation of its CARD domains. Our observation that FRET increases between LGP2 and NS3 after the addition of poly(I:C) in the cell as a whole (8A) but not specifically at the mitochondria (8C) does not support the hypothesis that LGP2 is acting alone to shuttle NS3. It is possible, however, that both LGP2 and MDA5 might be necessary to localize NS3 to mitochondria to catalyze MAVS cleavage. Such an idea warrants further study.

Experimental procedures

Materials

Standard techniques were used to generate expression plasmids encoding each fluorescently tagged helicase, as outlined below. Oligonucleotides were purchased from Integrated DNA Technologies (Coralville, IA).

pCMV-YFP-LGP2, *pCMV-CMV-LGP2-LGP2* (DHX58) cDNA was amplified using PCR from pCMV3-RC204837 (OriGene, Inc.) primers, which contain HindIII and XhoI restriction sites. The PCR product was then cut with XhoI and HindIII and ligated into a similarly treated pCMV6-AN-mYFP or pCMV6-AN-mCFP plasmid.

pCMV-YFP-RIG-I, *pCMV-CFP-RIG-I*—Vectors were purchased from GeneCopoeia (Rockville, MD) (catalog nos. EX-T0237-M15 and EX-T0237-M32).

pCMV-CFP-MDA5, *pCMV-YFP-MDA5*—Vectors were purchased from GeneCopoeia (Products EX-T0707-M15 and EX-T0707-M32).

pCMV-CFP-scNS3—scNS3 was amplified from the plasmid p28scNS3_1b(con1) (63) using primers that contain HindIII and XhoI restriction sites. The PCR product was then cut with XhoI and HindIII and ligated into a similarly treated pCMV6-AN-mCFP-LGP2 vector.

pCMV-CFP-NS3h—The NS3h open reading frame was cut out of p24a-NS3h_1b(con1) plasmid (64) using NheI and XhoI. The resulting fragment was gel-purified and ligated into similarly treated pCMV6-AN-scNS3.

pCMV-CFP-NS3—DNA encoding NS3 (HCV genotype 1b, con1 isolate) was cut out of p28-FL-NS3(1b_con1) (65) plasmid using the enzymes NheI and XhoI. The resulting cut FL NS3 product was gel-purified and ligated into pCMV-AN-scNS3, which was also cut with NheI and XhoI.

pCMV-CFP-NS3-4A—The NS3-NS4A open reading frame was excised from p28-His-NS3-4A-His (66) using NheI and XhoI. The resulting DNA fragment was gel-purified and ligated

Viral and cellular helicase interactions

into pCMV-AN-scNS3, which was also cut with NheI and XhoI.

pET24-YFP-NS3h—PCR primers were used to amplify the YFP open reading frame from the vector pCMV6-AN-mYFP (OriGene, Inc.). The amplicon was attached in frame with YFP using NdeI and NheI sites. Upon digestion, the fragment was ligated in to plasmid p24a-NS3h(con1) (64) that was also digested with NdeI and NheI and gel-purified.

pET24-CFP-NS3h—The CFP-NS3h open reading frame was excised from pCMV-CFP-NS3h (above) using EcoRI, purified, and ligated into a similarly treated pET24d vector (Novagen, Inc.).

Protein purification

YFP-NS3h and CFP-NS3h, used for calibration curves (see below), were purified from BL21(DE3) *Escherichia coli* containing either pET24-CFP-NS3h or pET24-YFP-NS3h using the same procedure that was described in detail previously (63).

Transfections with plasmids

293T cells grown to 90% confluence in 10-cm cell culture dishes under 37 °C and 5% CO₂ in Dulbecco's modified Eagle's medium/high glucose with L-glutamine, sodium pyruvate (GE Healthcare, product number SH30243), and supplemented FBS and non-essential amino acids at 10% and 1×, respectively. 100× penicillin/streptomycin (Thermo Fisher Scientific) was also added to all cultures at 1× final concentration. 2.0 × 10⁵ cells were seeded in 2 ml to 35-mm number 1.5 coverglass (0.16–0.19 mm) poly-D-lysine-coated glass bottom culture dishes containing a 14-mm diameter Microwell (MatTek Corp., Ashland, MA), incubated for 24 h at 37 °C under 5% CO₂. Aliquots of 1.5 μg of each plasmid were added along with 5 μl of TurboFect Transfection Reagent (Thermo Fisher Scientific) to 600 μl of serum-free DMEM. After 1 h at 23 °C, the entire solution was then added to the above cells. Then the dishes were returned to 37 °C and 5% CO₂ for 24 h to express the recombinant fluorescent protein construct.

Transfections with poly(I:C)

Four hours before imaging, either 200 μl of poly(I:C) (5 ng/μl) in DMEM plus TurboFect (1:100 dilution) or 200 μl of serum-free DMEM plus TurboFect (1:100 dilution) was added to the dishes containing transfected cells. The plates were then returned to the 37 °C, 5% CO₂ incubator for 4 h. To remove phenol red, the cell medium was removed using aspiration and replaced with prewarmed serum-free DMEM lacking phenol red.

To stain mitochondria, cell medium was again removed, and cells were stained in 1 ml of 25 ng/ml MitoTracker Red (Thermo Fisher Scientific) in prewarmed serum-free DMEM lacking phenol red for 15 min. Cell medium was removed using aspiration and replaced with prewarmed serum-free DMEM lacking phenol red.

Cell-based protease assay

A MAVS-based reporter assay was used for a cell-based protease assay. 293T cells were co-transfected with plasmids

encoding NS3 and the plasmid TRIP-RFP-NLS-IPS (Charles M. Rice, Rockefeller University), which encodes the “TagRFP” red fluorescent protein (RFP, Evrogen, Inc.) and an SV40 NLS fused to residues 462–540 of MAVS (also known as IPS) (35). Cells were imaged as described below.

ISRE assays

3.0 × 10⁴ of HEK293T cells/well were plated per well of a 24-well plate. After 12 h at 37 °C, 0.5 μg of the pISRE-luc (Agilent Technologies, Inc., catalog no. 219092) plasmid expressing firefly luciferase under control of and interferon-stimulated regulatory element was co-transfected along with either 0.5 μg of plasmid expressing YFP alone or YFP-RIG-I, YFP-MDA5, or YFP-LGP2 using TurboFect (as above). After 24 h at 37 °C, luciferase activity was measured using the Firefly Luc One-Step Flow Assay Kit (Pierce).

Two-photon fluorescence microspectroscopy

Images were obtained at room temperature of cells described above using a two-photon microspectroscopy comprising a Nikon Eclipse TiTM (Nikon Instruments Inc., Melville, NY) inverted microscope stand and an OptiMiS scanning/detection head (Aurora Spectral Technologies, Grafton, WI). A mode-locked laser (MaiTaiTM, Spectra Physics, Santa Clara, CA) was used for fluorescence excitation. It produces 100-fs pulses with wavelengths tunable between 690 and 1040 nm with an ~7-nm full-width half-maximum. The OptiMiS detection head was modified to include a line-scan protocol (10) and the ability to automatically change the excitation wavelength while maintaining constant power (13). The line-scan protocol allows for signals 2 orders of magnitude larger than a point-scan approach for the same line-dwell time. This improves accuracy by reducing photobleaching (10). The laser light was focused through an infinity-corrected oil-immersion objective (100× magnification, numerical aperture = 1.45; Nikon Instruments Inc.). The fluorescence was detected using a non-descanned detection scheme, whereby light is projected through a transmission grating onto a cooled electron-multiplying CCD (EMCCD) camera (iXon X3 897, Andor Technologies, Belfast, UK). The dispersed fluorescence (*i.e.* spectrum) strikes the CCD camera in a direction perpendicular to the excitation line. The spectral wavelengths are separated as a function of pixel position on the EMCCD array. This allows for the capture of three-dimensional information; two dimensions are the physical dimensions (440 × 300 pixels), and the third dimension is wavelength. Each spectrum is sampled at 200 different wavelengths. The emission channels range from ~400 to 600 nm with a spectral resolution of ~1 nm. The custom software used to control the optical scanning head and EMCCD was written in C++ and developed in-house.

Q-MSI

As described previously in more detail (67), before each experiment, the microscope's spectral calibration was performed using 10 μM uranine and rhodamine standards, which allowed for the assignment of each wavelength to a known camera pixel (or detection channel). Two-photon microspectroscopic images were collected for 293T cells either singly or dou-

bly transfected with YFP- and/or CFP-tagged proteins. The CFP-tagged proteins served as donors of energy, whereas the YFP-tagged ones were used as acceptors of energy in FRET experiments. The singly expressing cells were imaged to obtain the elementary spectra (*i.e.* emission spectra divided by the maximum emission intensity) of the donor and the acceptor, whereas a sample expressing no fluorescent proteins but stained with MitoTracker was used to determine the elementary spectrum of MitoTracker.

For each combination of CFP- and YFP-tagged proteins, two scans were performed: a “FRET scan” using the peak excitation wavelength of the donor ($\lambda_{ex,1} = 840$ nm), in which the donor is primarily excited, and an “acceptor scan” at the peak excitation wavelength of the acceptor ($\lambda_{ex,1} = 960$ nm) in which the acceptor is maximally excited. A range of 15–30 fields of view were collected for each dish analyzed. The total acquisition time for a full set of microspectroscopic images (*i.e.* two sets of images each containing 440×300 pixels and 20 wavelengths/pixel) was ~ 60 s (10 s for each excitation scan and ~ 40 for changing the laser wavelength). Because the laser beam was shaped into a line at the sample plane, hundreds of voxels (the volume of the pixel measured) in the sample were excited simultaneously; the length of the line in the sample extended 3 times wider than the detectable region of the camera, such that in the field of view, the excitation power was approximately uniform. The typical laser power used was 200 milliwatts/line (or 0.13 milliwatts/excitation voxel) for both the first and the second scan; these powers were automatically controlled by a power-control module described previously (13). The pixel-level composite spectra acquired during the two acquisition scans were deconvoluted (*i.e.* unmixed) (42), assuming that each measured spectrum, S^m , is given by a linear combination of spectral components,

$$S^m(\lambda_{ex,i}, \lambda_{em}) = \sum_l (k^l(\lambda_{ex,i}) s^l(\lambda_{em})) \quad (\text{Eq. 1})$$

where i ($= 1, 2$) is the excitation wavelength index, and l is a summation index for the differing spectral species present in the sample, which in this work are the following: donor in the presence of acceptor ($l = DA$), acceptor in the presence of donor ($l = AD$), and, in some of the measurements, MitoTracker ($l = M$). In practice, there is also a constant (*i.e.* wavelength-independent) component of the measured spectrum, which appears as a nearly uniform background to each image acquired ($l = B$). Although we explicitly include that in the spectral unmixing, we shall ignore it hereafter, because it is not included in the determination of FRET efficiency or concentrations.

The abundance coefficients, k^{AD} , k^{DA} , and k^M , which are proportional to the emission intensities of the above-mentioned fluorescent species, were extracted using a general least-squares minimization algorithm described previously (13). Averages of the abundance coefficients taken over entire ROIs were then used to compute the total number of photons detected for the donors ($F^{DA}(\lambda_{ex,i}) = k^{DA}(\lambda_{ex,i}) w^D$), acceptors ($F^{AD}(\lambda_{ex,i}) = k^{AD}(\lambda_{ex,i}) w^A$), MitoTracker ($F^M(\lambda_{ex,i}) = k^M(\lambda_{ex,i}) w^M$), etc., using the spectral integrals (or the areas under each elementary spectrum) denoted by w with various superscripts.

These values were then used to calculate, using two equations derived previously (12, 13), the ROI-averaged donor fluorescence in the absence of acceptor (or FRET),

$$F^D(\lambda_{ex,1}) = F^{DA}(\lambda_{ex,1}) + \frac{Q^D}{Q^A} F(\lambda_{ex,1}, \lambda_{ex,2}) \quad (\text{Eq. 2})$$

and the ROI-averaged acceptor fluorescence in the absence of FRET (*i.e.* as if it were the result of direct excitation with laser light),

$$F^A(\lambda_{ex,2}) = \frac{F(\lambda_{ex,1}, \lambda_{ex,2})}{\rho^A - \rho^D} \quad (\text{Eq. 3})$$

where $F(\lambda_{ex,1}, \lambda_{ex,2}) \equiv F^{AD}(\lambda_{ex,1}) - \rho^A F^A(\lambda_{ex,2})$, $\rho^A \equiv \Gamma^{\lambda_{ex,1}A} / \Gamma^{\lambda_{ex,2}A}$, and $\rho^D \equiv \Gamma^{\lambda_{ex,1}D} / \Gamma^{\lambda_{ex,2}D}$.

The average, over a specific ROI, of apparent FRET efficiency (E_{app}), defined here as the ratio of the donor fluorescence lost through FRET and the donor fluorescence in the absence of FRET, was computed from the above parameters using the following equation.

$$E_{app} = 1 - \frac{F^{DA}(\lambda_{ex,1})}{F^D(\lambda_{ex,1})} \quad (\text{Eq. 4})$$

Last, the total concentrations of donor-tagged proteins, $[D]$, and acceptor-tagged proteins, $[A]$, residing in each sample voxel (corresponding to each image pixel) were obtained via calibration of the pixel-level values of $F^D(\lambda_{ex,1})$ and $F^A(\lambda_{ex,2})$ using 10-fold dilution series of solutions of purified CFP-NS3h (D) and YFP-NS3h (A) proteins; fluorescence data of both the protein solutions and the 293T cells were acquired using the exact same imaging conditions. To perform the calibration, plots of $F^D(\lambda_{ex,1})$ versus CFP-NS3h concentration and $F^A(\lambda_{ex,2})$ versus YFP-NS3h concentration were constructed. The slopes of the CFP-NS3h and YFP-NS3h dilution curves, corresponding to the number of fluorescence counts per micromolar solution, were found to be 958 and 5,317, respectively. The voxel was calculated to be 3.13×10^{-17} liters (68). More details on this calibration are given elsewhere (13). The pixel-level total concentrations were averaged over regions of interest to obtain the average concentrations of donors and acceptors.

Author contributions—M. J. C., D. N. F., and V. R. designed the experiments and wrote the manuscript. M. J. C. performed the experiments. R. K. provided key reagents and helped conceive the study. M. S. and V. R. derived key equations. M. S., G. B., and J. D. P. assisted with Q-MSI data analysis. All authors have given approval to the final version of the manuscript.

Acknowledgments—We thank Angel Corona, Diana Kornov, Emily Oja, Kou Yang, Caleb Mrozinsky, and Dammar Badu for valuable technical assistance and helpful discussions and Karyn M. Frick and Sergei Kuchin for help with statistical analyses.

References

1. Abdel-Monem, M., and Hoffmann-Berling, H. (1976) Enzymic unwinding of DNA. 1. Purification and characterization of a DNA-dependent ATPase from *Escherichia coli*. *Eur. J. Biochem.* **65**, 431–440

2. Li, N., Zhai, Y., Zhang, Y., Li, W., Yang, M., Lei, J., Tye, B. K., and Gao, N. (2015) Structure of the eukaryotic MCM complex at 3.8 Å. *Nature* **524**, 186–191
3. Singleton, M. R., Sawaya, M. R., Ellenberger, T., and Wigley, D. B. (2000) Crystal structure of T7 gene 4 ring helicase indicates a mechanism for sequential hydrolysis of nucleotides. *Cell* **101**, 589–600
4. Itsathiphaisarn, O., Wing, R. A., Eliason, W. K., Wang, J., and Steitz, T. A. (2012) The hexameric helicase DnaB adopts a nonplanar conformation during translocation. *Cell* **151**, 267–277
5. Skordalakes, E., and Berger, J. M. (2006) Structural insights into RNA-dependent ring closure and ATPase activation by the Rho termination factor. *Cell* **127**, 553–564
6. Gu, M., and Rice, C. M. (2010) Three conformational snapshots of the hepatitis C virus NS3 helicase reveal a ratchet translocation mechanism. *Proc. Natl. Acad. Sci. U.S.A.* **107**, 521–528
7. Jennings, T. A., Mackintosh, S. G., Harrison, M. K., Sikora, D., Sikora, B., Dave, B., Tackett, A. J., Cameron, C. E., and Raney, K. D. (2009) NS3 helicase from the hepatitis C virus can function as a monomer or oligomer depending on enzyme and substrate concentrations. *J. Biol. Chem.* **284**, 4806–4814
8. Sikora, B., Chen, Y., Licht, C. F., Harrison, M. K., Jennings, T. A., Tang, Y., Tackett, A. J., Jordan, J. B., Sakon, J., Cameron, C. E., and Raney, K. D. (2008) Hepatitis C virus NS3 helicase forms oligomeric structures that exhibit optimal DNA unwinding activity *in vitro*. *J. Biol. Chem.* **283**, 11516–11525
9. Raicu, V., Stoneman, M. R., Fung, R., Melnichuk, M., Jansma, D. B., Pisterzi, L. F., Rath, S., Fox, M., Wells, J. W., and Saldin, D. K. (2009) Determination of supramolecular structure and spatial distribution of protein complexes in living cells. *Nature Photonics* **3**, 107–113
10. Biener, G., Stoneman, M. R., Acbas, G., Holz, J. D., Orlova, M., Komarova, L., Kuchin, S., and Raicu, V. (2013) Development and experimental testing of an optical micro-spectroscopic technique incorporating true line-scan excitation. *Int. J. Mol. Sci.* **15**, 261–276
11. Raicu, V., and Singh, D. R. (2013) FRET spectrometry: a new tool for the determination of protein quaternary structure in living cells. *Biophys. J.* **105**, 1937–1945
12. King, C., Stoneman, M., Raicu, V., and Hristova, K. (2016) Fully quantified spectral imaging reveals *in vivo* membrane protein interactions. *Integr. Biol.* **8**, 216–229
13. Stoneman, M. R., Paprocki, J. D., Biener, G., Yokoi, K., Shevade, A., Kuchin, S., and Raicu, V. (2016) Quaternary structure of the yeast pheromone receptor Ste2 in living cells. *Biochim. Biophys. Acta* **10.1016/j.bbame.2016.12.008**
14. Byrd, A. K., and Raney, K. D. (2012) Superfamily 2 helicases. *Front. Biosci.* **17**, 2070–2088
15. Frick, D. N. (2007) The hepatitis C virus NS3 protein: a model RNA helicase and potential drug target. *Curr. Issues Mol. Biol.* **9**, 1–20
16. Seth, R. B., Sun, L., Ea, C. K., and Chen, Z. J. (2005) Identification and characterization of MAVS, a mitochondrial antiviral signaling protein that activates NF- κ B and IRF 3. *Cell* **122**, 669–682
17. Reikine, S., Nguyen, J. B., and Modis, Y. (2014) Pattern recognition and signaling mechanisms of RIG-I and MDA5. *Front. Immunol.* **5**, 342
18. Fitzgerald, M. E., Rawling, D. C., Vela, A., and Pyle, A. M. (2014) An evolving arsenal: viral RNA detection by RIG-I-like receptors. *Curr. Opin. Microbiol.* **20**, 76–81
19. Errett, J. S., and Gale, M. (2015) Emerging complexity and new roles for the RIG-I-like receptors in innate antiviral immunity. *Virology* **30**, 163–173
20. Horner, S. M., and Gale, M. (2013) Regulation of hepatic innate immunity by hepatitis C virus. *Nat. Med.* **19**, 879–888
21. Walker, J. E., Saraste, M., Runswick, M. J., and Gay, N. J. (1982) Distantly related sequences in the α - and β -subunits of ATP synthase, myosin, kinases and other ATP-requiring enzymes and a common nucleotide binding fold. *EMBO J.* **1**, 945–951
22. Uchikawa, E., Lethier, M., Malet, H., Brunel, J., Gerlier, D., and Cusack, S. (2016) Structural analysis of dsRNA binding to anti-viral pattern recognition receptors LGP2 and MDA5. *Mol. Cell* **62**, 586–602
23. Mackintosh, S. G., Lu, J. Z., Jordan, J. B., Harrison, M. K., Sikora, B., Sharma, S. D., Cameron, C. E., Raney, K. D., and Sakon, J. (2006) Structural and biological identification of residues on the surface of NS3 helicase required for optimal replication of the hepatitis C virus. *J. Biol. Chem.* **281**, 3528–3535
24. Wu, B., Peisley, A., Tetrault, D., Li, Z., Egelman, E. H., Magor, K. E., Walz, T., Penczek, P. A., and Hur, S. (2014) Molecular imprinting as a signal-activation mechanism of the viral RNA sensor RIG-I. *Mol. Cell* **55**, 511–523
25. Bruns, A. M., Pollpeter, D., Hadizadeh, N., Myong, S., Marko, J. F., and Horvath, C. M. (2013) ATP hydrolysis enhances RNA recognition and antiviral signal transduction by the innate immune sensor, laboratory of genetics and physiology 2 (LGP2). *J. Biol. Chem.* **288**, 938–946
26. Bruns, A. M., Leser, G. P., Lamb, R. A., and Horvath, C. M. (2014) The innate immune sensor LGP2 activates antiviral signaling by regulating MDA5-RNA interaction and filament assembly. *Mol. Cell* **55**, 771–781
27. Bruns, A. M., and Horvath, C. M. (2015) LGP2 synergy with MDA5 in RLR-mediated RNA recognition and antiviral signaling. *Cytokine* **74**, 198–206
28. Foy, E., Li, K., Sumpter, R., Jr., Loo, Y. M., Johnson, C. L., Wang, C., Fish, P. M., Yoneyama, M., Fujita, T., Lemon, S. M., and Gale, M., Jr. (2005) Control of antiviral defenses through hepatitis C virus disruption of retinoic acid-inducible gene-1 signaling. *Proc. Natl. Acad. Sci. U.S.A.* **102**, 2986–2991
29. Lin, R., Lacoste, J., Nakhaei, P., Sun, Q., Yang, L., Paz, S., Wilkinson, P., Julkunen, I., Vitour, D., Meurs, E., and Hiscott, J. (2006) Dissociation of a MAVS/IPS-1/VISA/Cardif-IKK ϵ molecular complex from the mitochondrial outer membrane by hepatitis C virus NS3-4A proteolytic cleavage. *J. Virol.* **80**, 6072–6083
30. Louber, J., Kowalinski, E., Bloyet, L. M., Brunel, J., Cusack, S., and Gerlier, D. (2014) RIG-I self-oligomerization is either dispensable or very transient for signal transduction. *PLoS One* **9**, e108770
31. Cubitt, A. B., Heim, R., Adams, S. R., Boyd, A. E., Gross, L. A., and Tsien, R. Y. (1995) Understanding, improving and using green fluorescent proteins. *Trends Biochem. Sci.* **20**, 448–455
32. Day, R. N., and Davidson, M. W. (2009) The fluorescent protein palette: tools for cellular imaging. *Chem. Soc. Rev.* **38**, 2887–2921
33. Heim, R., Prasher, D. C., and Tsien, R. Y. (1994) Wavelength mutations and posttranslational autooxidation of green fluorescent protein. *Proc. Natl. Acad. Sci. U.S.A.* **91**, 12501–12504
34. Miyawaki, A., Griesbeck, O., Heim, R., and Tsien, R. Y. (1999) Dynamic and quantitative Ca²⁺ measurements using improved cameleons. *Proc. Natl. Acad. Sci. U.S.A.* **96**, 2135–2140
35. Jones, C. T., Catanese, M. T., Law, L. M., Khetani, S. R., Syder, A. J., Ploss, A., Oh, T. S., Schoggins, J. W., MacDonald, M. R., Bhatia, S. N., and Rice, C. M. (2010) Real-time imaging of hepatitis C virus infection using a fluorescent cell-based reporter system. *Nat. Biotechnol.* **28**, 167–171
36. Sanchez David, R. Y., Combredet, C., Sismeiro, O., Dillies, M. A., Jagla, B., Coppée, J. Y., Mura, M., Guerbois Galla, M., Despres, P., Tangy, F., and Komarova, A. V. (2016) Comparative analysis of viral RNA signatures on different RIG-I-like receptors. *Elife* **5**, e11275
37. Pichlmair, A., Schulz, O., Tan, C. P., Näslund, T. I., Liljeström, P., Weber, F., and Reis e Sousa, C. (2006) RIG-I-mediated antiviral responses to single-stranded RNA bearing 5'-phosphates. *Science* **314**, 997–1001
38. Rehwinkel, J., Tan, C. P., Goubau, D., Schulz, O., Pichlmair, A., Bier, K., Robb, N., Vreede, F., Barclay, W., Fodor, E., and Reis e Sousa, C. (2010) RIG-I detects viral genomic RNA during negative-strand RNA virus infection. *Cell* **140**, 397–408
39. Patel, J. R., Jain, A., Chou, Y. Y., Baum, A., Ha, T., and García-Sastre, A. (2013) ATPase-driven oligomerization of RIG-I on RNA allows optimal activation of type-I interferon. *EMBO Rep.* **14**, 780–787
40. Zhang, H. X., Liu, Z. X., Sun, Y. P., Zhu, J., Lu, S. Y., Liu, X. S., Huang, Q. H., Xie, Y. Y., Zhu, H. B., Dang, S. Y., Chen, H. F., Zheng, G. Y., Li, Y. X., Kuang, Y., Fei, J., *et al.* (2013) RIG-I regulates NF- κ B activity through binding to NF- κ B1 3'-UTR mRNA. *Proc. Natl. Acad. Sci. U.S.A.* **110**, 6459–6464
41. Deddouche, S., Goubau, D., Rehwinkel, J., Chakravarty, P., Begum, S., Maillard, P. V., Borg, A., Matthews, N., Feng, Q., van Kuppeveld, F. J., and

- Reis e Sousa, C. (2014) Identification of an LGP2-associated MDA5 agonist in picornavirus-infected cells. *Elife* **3**, e01535
42. Raicu, V., Jansma, D. B., Miller, R. J., and Friesen, J. D. (2005) Protein interaction quantified *in vivo* by spectrally resolved fluorescence resonance energy transfer. *Biochem. J.* **385**, 265–277
 43. Denk, W., Strickler, J. H., and Webb, W. W. (1990) Two-photon laser scanning fluorescence microscopy. *Science* **248**, 73–76
 44. Mishra, A. K., Mavlyutov, T., Singh, D. R., Biener, G., Yang, J., Oliver, J. A., Ruoho, A., and Raicu, V. (2015) The σ -1 receptors are present in monomeric and oligomeric forms in living cells in the presence and absence of ligands. *Biochem. J.* **466**, 263–271
 45. Vazquez, C., and Horner, S. M. (2015) MAVS coordination of antiviral innate immunity. *J. Virol.* **89**, 6974–6977
 46. Hou, F., Sun, L., Zheng, H., Skaug, B., Jiang, Q. X., and Chen, Z. J. (2011) MAVS forms functional prion-like aggregates to activate and propagate antiviral innate immune response. *Cell* **146**, 448–461
 47. Rodriguez, K. R., Bruns, A. M., and Horvath, C. M. (2014) MDA5 and LGP2: accomplices and antagonists of antiviral signal transduction. *J. Virol.* **88**, 8194–8200
 48. Berke, I. C., and Modis, Y. (2012) MDA5 cooperatively forms dimers and ATP-sensitive filaments upon binding double-stranded RNA. *EMBO J.* **31**, 1714–1726
 49. Peisley, A., Wu, B., Yao, H., Walz, T., and Hur, S. (2013) RIG-I forms signaling-competent filaments in an ATP-dependent, ubiquitin-independent manner. *Mol. Cell* **51**, 573–583
 50. Levin, M. K., and Patel, S. S. (1999) The helicase from hepatitis C virus is active as an oligomer. *J. Biol. Chem.* **274**, 31839–31846
 51. Murali, A., Li, X., Ranjith-Kumar, C. T., Bhardwaj, K., Holzenburg, A., Li, P., and Kao, C. C. (2008) Structure and function of LGP2, a DEX(D/H) helicase that regulates the innate immunity response. *J. Biol. Chem.* **283**, 15825–15833
 52. Martin, B. R., Giepmans, B. N., Adams, S. R., and Tsien, R. Y. (2005) Mammalian cell-based optimization of the biarsenical-binding tetracysteine motif for improved fluorescence and affinity. *Nat. Biotechnol.* **23**, 1308–1314
 53. Baril, M., Racine, M. E., Penin, F., and Lamarre, D. (2009) MAVS dimer is a crucial signaling component of innate immunity and the target of hepatitis C virus NS3/4A protease. *J. Virol.* **83**, 1299–1311
 54. Bruns, A. M., and Horvath, C. M. (2012) Activation of RIG-I-like receptor signal transduction. *Crit. Rev. Biochem. Mol. Biol.* **47**, 194–206
 55. Bruns, A. M., and Horvath, C. M. (2014) Antiviral RNA recognition and assembly by RLR family innate immune sensors. *Cytokine Growth Factor Rev.* **25**, 507–512
 56. Patowary, S., Pisterzi, L. F., Biener, G., Holz, J. D., Oliver, J. A., Wells, J. W., and Raicu, V. (2015) Experimental verification of the kinetic theory of FRET using optical microspectroscopy and obligate oligomers. *Biophys. J.* **108**, 1613–1622
 57. Singh, D. R., Mohammad, M. M., Patowary, S., Stoneman, M. R., Oliver, J. A., Movileanu, L., and Raicu, V. (2013) Determination of the quaternary structure of a bacterial ATP-binding cassette (ABC) transporter in living cells. *Integr. Biol.* **5**, 312–323
 58. Patowary, S., Alvarez-Curto, E., Xu, T. R., Holz, J. D., Oliver, J. A., Milligan, G., and Raicu, V. (2013) The muscarinic M3 acetylcholine receptor exists as two differently sized complexes at the plasma membrane. *Biochem. J.* **452**, 303–312
 59. Mishra, A. K., Gragg, M., Stoneman, M. R., Biener, G., Oliver, J. A., Miszta, P., Filipek, S., Raicu, V., and Park, P. S. (2016) Quaternary structures of opsin in live cells revealed by FRET spectrometry. *Biochem. J.* **473**, 3819–3836
 60. Foy, E., Li, K., Wang, C., Sumpter, R., Jr., Ikeda, M., Lemon, S. M., and Gale, M., Jr. (2003) Regulation of interferon regulatory factor-3 by the hepatitis C virus serine protease. *Science* **300**, 1145–1148
 61. Horner, S. M., Park, H. S., and Gale, M. (2012) Control of innate immune signaling and membrane targeting by the hepatitis C virus NS3/4A protease are governed by the NS3 helix α 0. *J. Virol.* **86**, 3112–3120
 62. Sumpter, R., Jr., Wang, C., Foy, E., Loo, Y. M., and Gale, M., Jr. (2004) Viral evolution and interferon resistance of hepatitis C virus RNA replication in a cell culture model. *J. Virol.* **78**, 11591–11604
 63. Frick, D. N., Ginzburg, O., and Lam, A. M. (2010) A method to simultaneously monitor hepatitis C virus NS3 helicase and protease activities. *Methods Mol. Biol.* **587**, 223–233
 64. Belon, C. A., and Frick, D. N. (2009) Fuel specificity of the hepatitis C virus NS3 helicase. *J. Mol. Biol.* **388**, 851–864
 65. Neumann-Haefelin, C., Frick, D. N., Wang, J. J., Pybus, O. G., Salloum, S., Narula, G. S., Eckart, A., Biezynski, A., Eiermann, T., Klenerman, P., Viazov, S., Roggendorf, M., Thimme, R., Reiser, M., and Timm, J. (2008) Analysis of the evolutionary forces in an immunodominant CD8 epitope in hepatitis C virus at a population level. *J. Virol.* **82**, 3438–3451
 66. Frick, D. N., Rypma, R. S., Lam, A. M., and Gu, B. (2004) The nonstructural protein 3 protease/helicase requires an intact protease domain to unwind duplex RNA efficiently. *J. Biol. Chem.* **279**, 1269–1280
 67. Stoneman, M., Singh, D., and Raicu, V. (2011) *In vivo* quantification of G protein coupled receptor interactions using spectrally resolved two-photon microscopy. *J. Vis. Exp.* 10.3791/2247.
 68. Zipfel, W. R., Williams, R. M., and Webb, W. W. (2003) Nonlinear magic: multiphoton microscopy in the biosciences. *Nat. Biotechnol.* **21**, 1369–1377

Quantitative microspectroscopic imaging reveals viral and cellular RNA helicase interactions in live cells

M. J. Corby, Michael R. Stoneman, Gabriel Biener, Joel D. Paprocki, Rajesh Kolli, Valerica Raicu and David N. Frick

J. Biol. Chem. 2017, 292:11165-11177.

doi: 10.1074/jbc.M117.777045 originally published online May 8, 2017

Access the most updated version of this article at doi: [10.1074/jbc.M117.777045](https://doi.org/10.1074/jbc.M117.777045)

Alerts:

- [When this article is cited](#)
- [When a correction for this article is posted](#)

[Click here](#) to choose from all of JBC's e-mail alerts

This article cites 68 references, 29 of which can be accessed free at <http://www.jbc.org/content/292/27/11165.full.html#ref-list-1>